Research Article Vol. 59, No. 17 / 10 June 2020 / Applied Optics 5335

applied optics

Flight model characterization of the wide-field off-axis telescope for the MATS satellite

Woojin Park,[1,7] Arvid Hammar,[2] Soojong Pak,[1,*] Seunghyuk Chang,[3] Jörg Gumbel,[4] Linda Megner,[4] Ole Martin Christensen,[4,5] Jordan Rouse,[2] and Dae Wook Kim[6]

[1]School of Space Research and Institute of Natural Sciences, Kyung Hee University, 1732 Deogyeong-daero, Giheung-gu, Yongin-si, Gyeonggi-do 17104, South Korea
[2]Omnisys Instruments AB, August Barks gata 6B, SE-421 32 Västra Frölunda, Sweden
[3]Center for Integrated Smart Sensors, 291 Daehak-ro, Yuseong-gu, Daejeon 34141, South Korea
[4]Department of Meteorology (MISU), Stockholm University, SE-106 91 Stockholm, Sweden
[5]Earth and Space Sciences, Chalmers University of Technology, SE-412 96 Gothenburg, Sweden
[6]James C. Wyant College of Optical Sciences, University of Arizona, 1630 E. University Blvd., Tucson, Arizona 85721, USA
[7]e-mail: woojinpark@khu.ac.kr
*Corresponding author: soojong@khu.ac.kr

Received 17 March 2020; accepted 11 May 2020; posted 14 May 2020 (Doc. ID 392187); published 10 June 2020

We present optical characterization, calibration, and performance tests of the Mesospheric Airglow/Aerosol Tomography Spectroscopy (MATS) satellite, which for the first time, to the best of our knowledge, for a satellite, applies a linear-astigmatism-free confocal off-axis reflective optical design. Mechanical tolerances of the telescope were investigated using Monte Carlo methods and single-element perturbations. The sensitivity analysis results indicate that tilt errors of the tertiary mirror and a surface RMS error of the secondary mirror mainly degrade optical performance. From the Monte Carlo simulation, the tolerance limits were calculated to ±0.5 mm, ±1 mm, and ±0.15° for decenter, despace, and tilt, respectively. We performed characterization measurements and optical tests with the flight model of the satellite. Multi-channel relative pointing, total optical system throughput, and distortion of each channel were characterized for end-users. Optical performance was evaluated by measuring the modulation transfer function (MTF) and point spread function (PSF). The final MTF performance was 0.25 MTF at 20 lp/mm for the ultraviolet channel (304.5 nm), and 0.25–0.54 MTF at 10 lp/mm for infrared channels. The salient fact of the PSF measurement of this system is that there is no noticeable linear astigmatism detected over a wide field of view (5.67° × 0.91°). All things considered, the design method showed great advantages in wide field of view observations with satellite-level optical performance.

https://doi.org/10.1364/AO.392187

1. INTRODUCTION

Mesospheric Airglow/Aerosol Tomography Spectroscopy (MATS) is a Swedish microsatellite mission that observes noctilucent clouds (NLCs) (80–86 km altitudes) and O_2 atmospheric band dayglow/nightglow (75–110 km altitudes) over a wide field of view (5.67° × 0.91°) in two ultraviolet (UV) channels and four infrared (IR) channels within a wavelength range between 270 and 772 nm [1]. The main optical system of the MATS satellite is the limb-viewing telescope, which is designed with a 35 mm entrance pupil diameter and a focal ratio of 7.4 [2,3]. The whole system includes three off-axis mirrors, beam splitters, broad/narrow bandpass filters, and six charge-coupled devices (CCDs) in the same compact limb housing (see Fig. 1). A confocal off-axis reflective system is adapted to the telescope design for diffraction limited optical performance over the full field of view. This optical design eliminates linear astigmatism without any correcting lenses, enabling wide field of view observations in a wide spectral range [4–6].

Tolerance analysis is generally performed before fabrication of the optical system to examine the feasibility of the optical design, but it is also required to confirm performance stability in satellite platform vibration environments [7]. Optical system characterization is also valuable for the final image corrections. Even though optical systems need to be calibrated during the mission [8,9], laboratory characterization measurements before launching are essential [10,11]. A distortion correction, especially, is crucial to increase accuracy of scientific results of the MATS satellite whose data use a tomography technique [12].

The linear-astigmatism-free (LAF) confocal off-axis reflective system has outstanding performance in low distortion and field

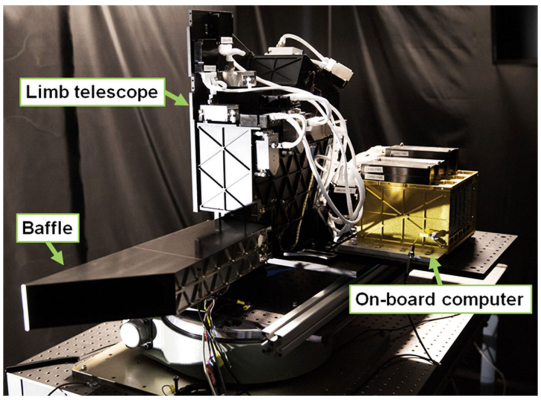

Fig. 1. Picture of the limb telescope with the baffle and the on-board computer.

curvature [13]. Performance of prototype LAF systems has been evaluated in previous research [14,15], but characterization measurements have not been performed. Optical performance measurements for one of the IR channels of the prototype telescope has already been done [3].

Since the limb telescope has six channels, performance and relative pointing accuracy for all channels must be carefully measured. All these tolerance analysis and characterization results can be utilized for the final imaging analysis.

In this paper, sensitivity analysis and Monte Carlo simulations performed for tolerance analysis are introduced in Section 2. Characterization of the telescope with total throughput, relative pointing, and distortion measurements of the system is introduced in Section 3. In Section 4, we show the imaging performance of the flight optics for two UV and four IR channels. All results are discussed and summarized in Section 5.

2. TOLERANCE ANALYSIS

Optical performance can be degraded by fabrication, assembly process, thermal conditions, vibration environments from the launch system, and satellite platform vibration environments, so tolerance analysis has been considered an important step in optical system development to improve reliability and practicality of the system [16,17]. The main objectives of tolerance analysis are to determine optical performance degradation due to external environments and to decide tolerance ranges of the system for fabrication and alignment [18].

Tolerancing parameters are x- and y-decenter, α-, β-, and γ-tilt, despace, and focus. Decenter and tilt are adapted to each mirror, while despace corresponds to inter-mirror distance [14]. The coordinate system for tolerance analysis is shown in Fig. 2. Since we adjust the focal position to get the best image, the performance degradataion from tolerances is compensated for by the focal position.

At the start, the individual tolerance budget of each parameter and its sensitivity are explored with sensitivity analysis. Then, a statistical analysis based on the Monte Carlo method is performed to assess system performance. Cumulative probability, which is the result of the Monte Carlo simulation, enables us to estimate the expected final system performance.

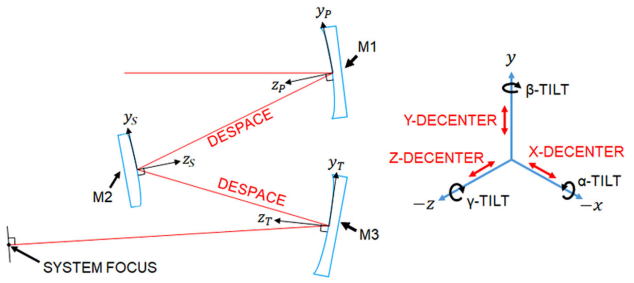

Fig. 2. Coordinate system for tolerance analysis.

A. Sensitivity Analysis

Optical component sensitivities are explored by individually implementing tolerance parameters [19]. The modulation transfer function (MTF) at 30 lp/mm is selected as the performance criterion, and the reference wavelength is set to 270 nm, which is the most sensitive channel to mirror surface errors. MTF values at five points within the field of view (i.e., $-2.84° \times -0.46°$, $-1.42° \times -0.23°$, $0.00° \times 0.00°$, $1.42° \times 0.23°$, $2.84° \times 0.46°$) are averaged for each tolerance parameter. Figure 3 illustrates sensitivity analysis results of each tolerance parameter. All parameters of M1 (primary mirror), M2 (secondary mirror), and M3 (tertiary mirror) correspond to red, blue, and magenta colors for plots (a)–(c), (e)–(g), and (i)–(k). Inter-mirror distances of M1-M2 and M2-M3 are indicated with green circles and green squares, respectively.

From the sensitivity analysis, we expect that α-tilt of M2, α- and β-tilt of M3, and surface RMS error of M2 are the parameters most critical for image quality degradation. On the other hand, the image quality is significantly less sensitive to γ-tilt and despace for all mirrors. In this system, α- or β-tilt of M3 is critical for image quality, so it can be set to the compensator for realignments.

B. Monte Carlo Simulation

Sensitivity analysis can provide performance sensitivity for each of the optical component errors. However, it is necessary to confirm the system tolerance limits when all tolerances simultaneously affect the system. The Monte Carlo method is the most common way to predict the cumulative probability for meeting specific performance requirements [20,21].

Initial tolerance limits are estimated from the root sum square of each parameter of three mirrors calculated from sensitivity analysis, and they are optimized within fabrication and alignment error budgets [22]. OpticStudio is used for the Monte Carlo simulation. Table 1 lists tolerance parameters and the final tolerance limits that are calculated using the iterative method. Tolerance limits are the same for all mirrors. Focus is selected as a compensator, and reference wavelength is the same as the one used in the sensitivity analysis.

Tolerance distributions for the Monte Carlo simulation follow a normal distribution. Figure 4 shows the histogram of 5000 Monte Carlo tries that are binned as a function of MTF. Required optical performance (i.e., 0.3 MTF) is met at 96% cumulative probability. From the sensitivity analysis of

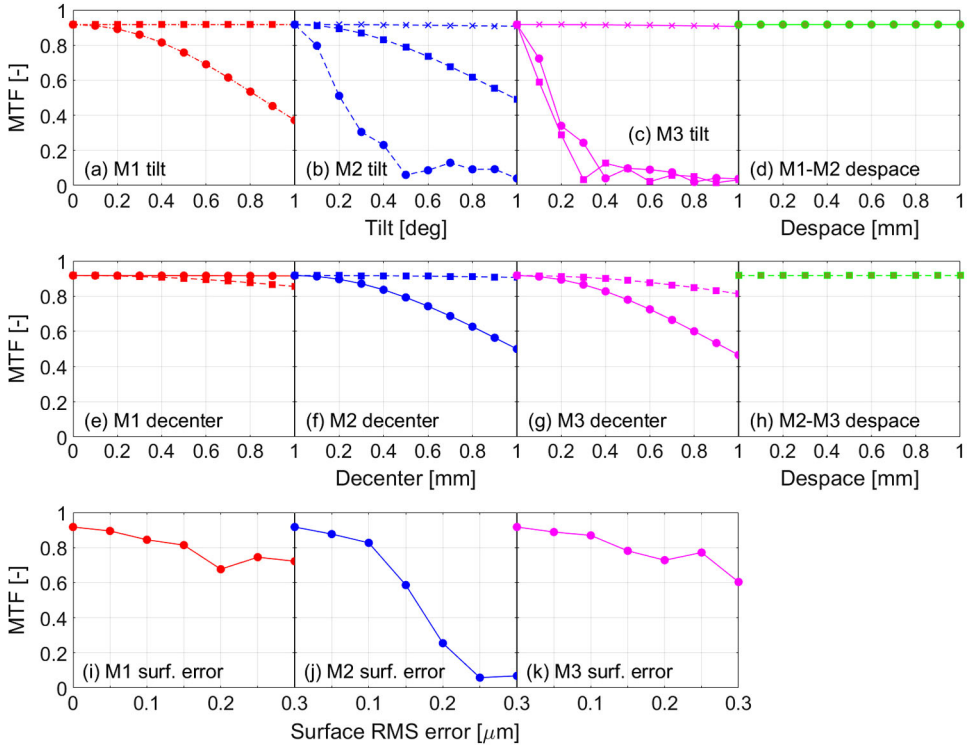

Fig. 3. Sensitivity analysis results of M1 (red), M2 (blue), and M3 (magenta): (a)–(c) α- (circle), β- (square), and γ- (cross) tilt, (e)–(g) x- (circle) and y- (square) decenter, (i)–(k) surface RMS error, (d) M1-M2 (circle), and (h) M2-M3 (square) despace. γ-tilt of M1 is overlapped with its β-tilt.

Table 1. Tolerance Limits for Monte Carlo Simulation

Parameter	Tolerance Limits[a]
x-, y-decenter	±0.5 mm
α-, β-tilt	±0.15°
Despace	±1.0 mm
Focus[b]	±1.0 mm

[a]Tolerance limits are the same for M1, M2, and M3.
[b]Focus is used as the compensator.

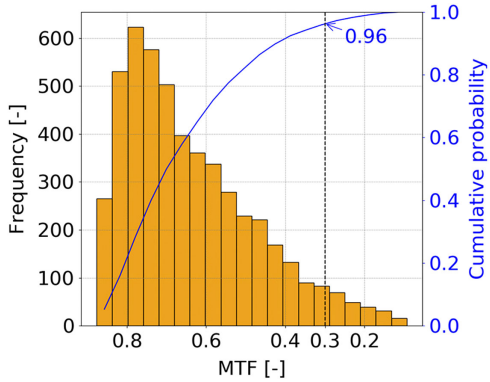

Fig. 4. Monte Carlo simulation results. The performance limit is indicated by a black dashed line. The blue solid line represents a cumulative probability curve.

the surface RMS errors, we expect that ~0.03 MTF could be additionally degraded when taking count the fabricated surface RMS errors, which are 0.049, 0.034, and 0.062 μm for M1, M2, and M3, respectively [3].

Tolerance limits of x- and y-decenter and α- and β-tilt are allowable ranges for the mission requirement when considering the mirror sizes that are 60 (L) mm × 40 (W) mm, 36 mm × 36 mm, and 90 mm × 80 mm for M1, M2, and M3, respectively. Nominal despace is ~250 mm for both M1-M2 and M2-M3. The tolerance limit of despace is less strict, since it rarely affects optical performance if focus compensations are mechanically available within ±1.0 mm [see Figs. 3(d) and 3(h)].

Tilt and decenter errors can be compensated for due to shims and L-brackets that are used to precisely position the mirrors and can be chosen in different thicknesses for relocations of the optical components.

3. SYSTEM CALIBRATION AND CHARACTERIZATION

Optical system calibration allows estimations of power and incident angles of the light entering the entrance pupil [23]. It considers not only systematic noise corrections that are bias, dark, and flat-field corrections in CCD data [24], but also characterization of total system throughput, relative pointing, distortion, etc. Calibrations for electronics of the limb house have been performed [25]. Systematic noise will be subtracted (bias and dark) and divided (flat) from the raw object frame after the data acquisition. The limb telescope has six channels and 19 optical components including mirrors, beam splitters, and

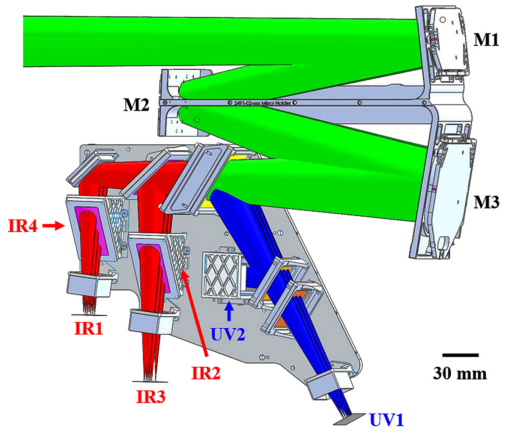

Fig. 5. Optical layout of the limb telescope. UV2, IR2, and IR4 CCDs are located at the backside of the instrument.

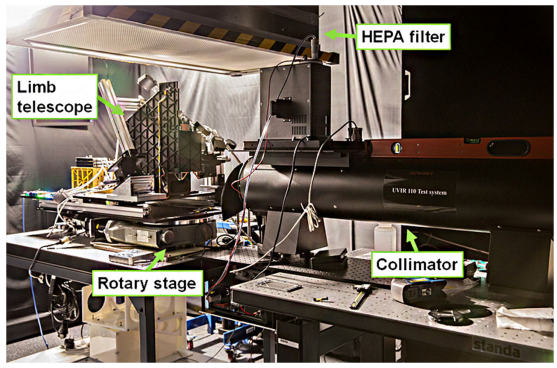

Fig. 6. Optical test setup for characterization and optical performance measurements. The limb telescope is installed under the HEPA filter and the fan (left side), and the collimator sits in front of the limb entrance aperture (right side).

broad and narrow bandpass filters. It is important to characterize total system throughput and relative pointing of each channel.

A. Total System Throughput

In the splitter box of the MATS telescope system, the incident beam from the off-axis telescope is split into six channels (see Fig. 5). Verification of transmittance and reflectivity of each optical component is necessary to calculate total throughput of the system and then to decide the CCD gain, exposure time, etc. Furthermore, reflectivity of diamond turned aluminum mirrors needs to be measured for characterization of the scattered light from high surface roughness mirrors [26,27].

Transmittance and reflectivity of filters and beam splitters have been measured by the component providers. We used the Andor iDus spectrometer and 1 kW Xenon lamp to measure specular reflectivity of the mirrors. Measurement results are listed in Table 2. Beam splitters, broadband filters, narrowband filters, and folding mirrors are abbreviated as BS, FB, FN, and FM, respectively. All the reflectivity and transmittance values are based on the central wavelength of each channel.

IR1 and IR2 show relatively high total throughput (>12%) while other channels have throughput between 3.2% and 6.2%. Low throughput is already expected by design. However, the MATS satellite observes the Earth's mesosphere, which is bright enough with the adequate CCD gain, and exposure time (~3 s). The three off-axis mirrors have UV enhanced aluminum coating. They are supposed to have 89% and 85% reflectivity for the UV and IR ranges, respectively [28]. The measurement results show that the mirror reflectivity in the UV channels is lower than our expectations, which might be the result of scattering caused by high surface roughness (~3 nm) [29].

B. Relative Pointing Characterization

Total throughput measurements and characterization of optical aberrations are common optical calibration tasks for telescopes [30], but relative pointing measurements are also necessary for multi-channel telescopes. As we mentioned in Section 1, two observation targets, NLCs and O_2 atmospheric band dayglow/nightglow, are located at different altitudes. For this reason, the image centers of UV and IR channels are different by design: the four IR channels should share their field of view, and so should the two UV channels.

There are relative pointing errors resulting from mechanical fabrication errors, filter or beam splitter misalignments, etc. Relative pointing measurements enable end-users to know and correct the pointing errors of each channel so that the proper targets can be observed. The relative pointing between the channels was measured by taking point source images that were generated by the 100 μm pinhole and the Inframet CDT11100HR collimator (Fig. 6) [31]. This optical test setup was also used for imaging performance measurements (Section 4).

Figure 7 displays the relative pointing of the IR and UV channels. Black crosses indicate the pointing reference of the satellite that is also considered as the optical axis of the telescope. Red and blue areas show targets for each channel. The field of view for each CCD is overlaid with colored solid lines.

Table 2. Bandpass, Reflectivity, and Transmittance of Optical Components[a]

Channel	WL (nm)	Mirror (-)	BS1 (-)	FB1 (-)	BS2 (-)	FM (-)	BS3 (-)	FN (-)	CCD QE (-)	Total (%)
UV1	270 ± 1.5	0.86	1.0 (R)	0.70	0.50 (T)	—	—	0.38	0.50	4.2
UV2	304.5 ± 1.5	0.80	1.0 (R)	0.69	0.51 (R)	0.79	—	0.41	0.55	3.2
IR1	762 ± 1.8	0.88	0.96 (T)	0.97	0.45 (T)	0.88	0.60 (T)	1.0	0.78	12
IR2	763 ± 4.0	0.88	0.96 (T)	0.97	0.55 (R)	—	0.75 (R)	0.98	0.78	20
IR3	754 ± 1.5	0.88	0.96 (T)	0.98	0.55 (R)	—	0.25 (T)	0.77	0.80	5.4
IR4	772 ± 1.5	0.88	0.96 (T)	0.98	0.45 (T)	0.88	0.40 (R)	0.81	0.76	6.2

[a]WL, wavelength; BS, beam splitter; FB, broadband filter; FN, narrowband filter; FM, folding mirror; QE, quantum efficiency; (R), reflectivity; (T), transmittance.

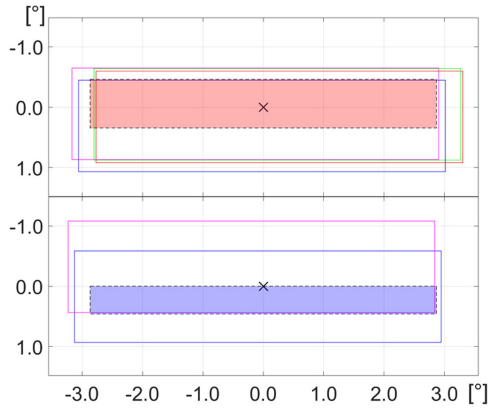

Fig. 7. Relative pointing of IR (top) and UV (bottom) channels. Field of view of IR1 (red), IR2 (magenta), IR3 (green), IR4 (blue), UV1 (blue), and UV2 (magenta) are illustrated with solid lines.

Table 3. Relative Pointing Offsets of UV and IR Targets[a]

Target/Channel	x-Offset (pix)[b]	y-Offset (pix)
UV source	0.00	77.60
UV1	−30.72	58.54
UV2	−66.56	−108.38
IR source	0.00	−19.40
IR1	89.79	54.47
IR2	−44.02	37.64
IR3	78.58	40.31
IR4	−7.49	104.92

[a]Offset values are relative to the pointing reference.
[b]The pixel size is 13.5 μm square for the E2V CCD42-10 CCD.

There are tight margins in the vertical direction, especially for UV channels. The IR channels seem to have good alignments while covering the target in all four channels. The maximum separations among IR channels are 0.2° in vertical and 0.4° in horizontal. UV channels are misaligned to the vertical direction by 0.5°, while they are horizontally misaligned by 0.1°. Even though UV fields are largely separated, they still properly cover their target.

The observed images should be aligned by using the relative pointing offset values listed in Table 3. The pointing reference (0.00, 0.00) corresponds to black crosses in Fig. 7. Due to different altitudes of UV and IR targets (70–90 km for UV, and 75–110 km for IR), y-offsets of each source deviate from 0.00 pixels.

C. Distortion

The MATS satellite will generate 3D cube data by using the tomography technique, which combines a bunch of images. Each frame will not match together if distortion exists, and it creates large errors in the tomography. Distortion is measured with the point source and a distortion target [31]. In this test, we accurately rotated the telescope into a specific angle, and compared the rotation angle with the incident angle of the beam derived from the image location at the sensor.

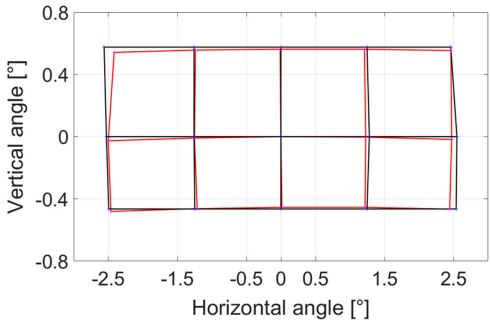

Fig. 8. Distortion measurements of the limb telescope. Black solid lines indicate the distortion grid by design, while red solid lines represent the measured distortion grid.

As the result shows in Fig. 8, there is pincushion-like distortion with more aberrations to the upper-left and the lower-right corners than to the other corners. The maximum distortions to vertical and horizontal directions are 2.57% and 3.70%, respectively. Distortions by design are 0.08% and 2.83% in vertical and horizontal directions, respectively.

Measured distortion can be generated by mirror surface figure errors that come mainly from the fabrication process and by filter bending caused by assembly stress.

4. IMAGING AND MTF PERFORMANCE

Imaging performance measurements took place in an ISO class 5 cleanroom. The limb instrument was installed on a rotary stage so that the optical tests could be performed not only at the image center, but also over full image fields (Figs. 1 and 6). Before we evaluated the optical performance, we precisely found focal positions by measuring 80% encircled energy diameter (EED) of point source images.

The 1951 USAF target is a good indicator for finding the approximate focus and for visually inspecting the optical performance. Figure 9 shows the USAF target images in UV2, IR1, IR2, IR3, and IR4 displaying clearly three individual bars at group 0 element 4 and group 1 element 4 in all channels, fulfilling the requirements of the IR channels. For the UV channels, it is required that the lines can be separated for group 2 element 4. Looking at Fig. 9(a), one can see that this requirement is fulfilled for channel UV1. It was not possible to take a USAF target image in UV1 due to extremely low transmission of the target in a 270 ± 1.5 nm wavelength band.

To determine the MTF, a slanted edge test target was used. Sharpness of the edge across the image position can be expressed with the edge spread function (ESF). It is transformed into line spread function (LSF) by taking a derivative of the ESF. The final MTF curves are derived by taking the Fourier transform and normalizing it [32–36].

The MTF measurements show that we have the best image resolution in UV2 followed by IR2, IR3, IR1, and IR4 (Fig. 10). Measured MTF performance is 0.25 MTF at 20 lp/mm for UV2, and 0.25, 0.29, 0.44, and 0.54 MTF at 10 lp/mm for IR4, IR1, IR3, and IR2, respectively. The MTF curve for UV1 was not available for measuring because of the low UV1 transmission to the slanted edge target.

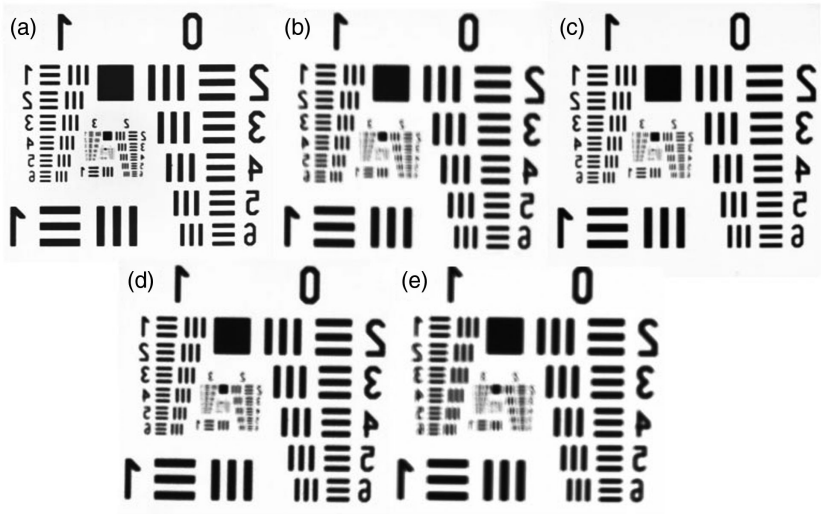

Fig. 9. USAF target images from the limb telescope in (a) UV2, (b) IR1, (c) IR2, (d) IR3, and (e) IR4. A USAF image in UV1 does not exist because of the low transmission of the target in the 270 ± 1.5 nm wavelength.

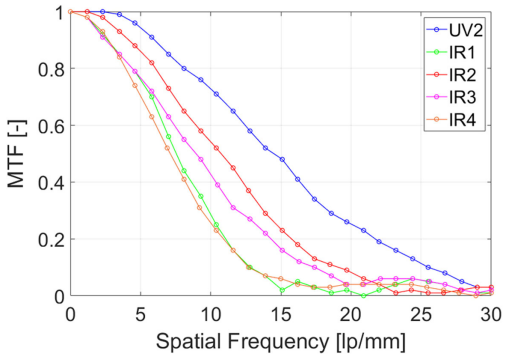

Fig. 10. Measured MTF curves of UV and IR channels except for UV1.

Instead, we evaluated the performance in UV1 with a point source image by comparing it to that of other channels. Measured spot sizes are listed in Table 4. As we expected from the MTF chart, UV2 has the smallest spot size out of all the channels. The performances among the channels for MTF and 80% EED follow the same trend except for IR1. The difference is caused by the big pixel size of the CCD (i.e., 13.5 μm), which implies that the pixel coverage of the point source image is only two to three pixels, making it difficult to estimate the exact spot size. UV1 has the biggest spot size among the six channels. If we consider uncertainty from undersampling of 80% EED, the actual optical performance for UV1 will approximately equal that of IR4.

Optical performances have been evaluated at the center of the field of view. However, we also need to figure out the performance over a full field of view since the LAF off-axis system has advantages, especially in wide field of view systems [37].

The whole limb instrument was rotated with a rotational axis at the center of the M1 surface for the full field of view tests. Figure 11 illustrates full field of view test results in IR2. As we can clearly see in the figure, there are no dominant off-axis aberrations detected over a full field of view. The geometry of

Table 4. 80% EED of 100 μm Point Source Images

Channel	WL (nm)	80% EED (μm)
UV1	270 ± 1.5	57.81
UV2	304.5 ± 1.5	26.72
IR1	762 ± 1.8	33.85
IR2	763 ± 4.0	38.19
IR3	754 ± 1.5	38.94
IR4	772 ± 1.5	48.22

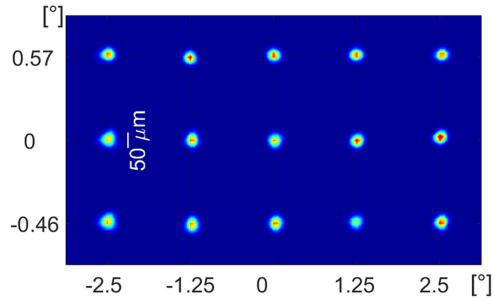

Fig. 11. Full field imaging results with the 100 μm pinhole in IR2. The white scale bar indicates 50 μm.

the spot images is almost uniform, while optical performance degradations are not noticeable, indicating that field curvature is negligible. As all channels share the same mirror system, off-axis aberrations in other channels will show a pattern similar to that of IR2.

5. DISCUSSION AND SUMMARY

The limb telescope is the main optical system of the MATS satellite. In this study we performed sensitivity analysis and Monte Carlo simulations to estimate the expected stability and performance of the telescope in space. Total system throughput and relative pointing are characterized for the multi-channel

imaging system. Optical performance is evaluated with the flight instrument not only at the image center but also over the full field of view.

System tolerance limits were decided by sensitivity analysis and an iterative method using Monte Carlo simulation. From the sensitivity analysis, we conclude that α-tilt and β-tilt of M3 are suitable compensators for alignment errors. Monte Carlo simulation results indicate the instrument has a 96% cumulative probability of meeting its required 0.3 MTF. The simulation does not include surface RMS errors of mirrors. From the sensitivity analysis results, however, the surface errors of fabricated flight mirrors, which are 0.034–0.062 μm, barely degrade the optical resolution.

Total system throughput is calculated by measuring reflectivity and transmittance of all optical components. Mirror reflectivity in UV wavelength is 3%–9% lower than our expectations, a discrepancy that likely resulted from scattering from the diamond turned mirror surface. Relative pointing measurements imply that despite the large vertical offset of UV2 (due to filter misalignment), all IR and UV CCDs can simultaneously cover their targets.

For the distortion measurements, a distortion lager than distortion by design is detected in the system. This additional distortion is caused by combinations of mirror surface errors and filter bending by assembly stress. However, due to our characterization results, these distortions can be corrected in the final scientific product.

We also measured the optical resolution and found that measured MTF performance is 0.25 MTF at 20 lp/mm for UV2 and 0.25–0.54 MTF at 10 lp/mm for IR channels. The results from UV1 are highly uncertain with a measured 80% EED spot size of 57.81 μm, which is less than the required resolution. However, these may be due to the low signal-to-noise ratio from the low power of the collimator lamp at 270 nm wavelength.

Linear astigmatism and field curvature are not detected in the full field of view image. Since the optical design has been optimized to reduce third-order aberrations, we have almost uniform optical performance over a large field of view.

In summation, we performed flight model characterizations and performance tests of the MATS satellite. The satellite applies the LAF confocal off-axis reflective optical design for the first time. It proves that building the LAF off-axis system is feasible with the satellite-level optical performance. The optical design and testing method introduced in this paper are applicable to any other optical applications.

Funding. Swedish National Space Agency; National Research Council of Science and Technology (CAP–15–01–KBSI).

Acknowledgment. This work was a collaborative research work with the Wyant College of Optical Sciences for its assistance with the linear-astigmatism-free, three-mirror system development. This research was made possible in part by the Technology Research Initiative Fund Optics/Imaging Program at the University of Arizona.

Disclosures. The authors declare no conflicts of interest.

REFERENCES

1. J. Gumbel, L. Megner, O. M. Christensen, S. Chang, J. Dillner, T. Ekebrand, G. Giono, A. Hammar, J. Hedin, N. Ivchenko, B. Karlsson, M. Kruse, A. Li, S. McCallion, D. P. Murtagh, G. Olentšenko, S. Pak, W. Park, J. Rouse, J. Stegman, and G. Witt, "The MATS satellite mission—gravity waves studies by mesospheric airglow/aerosol tomography and spectroscopy," Atmos. Chem. Phys. **20**, 431–445 (2020).
2. A. Hammar, O. M. Christensen, W. Park, S. Pak, A. Emrich, and J. Stake, "Stray light suppression of a compact off-axis telescope for a satellite-borne instrument for atmospheric research," Proc. SPIE **10815**, 108150F (2018).
3. A. Hammar, W. Park, S. Chang, S. Pak, A. Emrich, and J. Stake, "Wide-field off-axis telescope for the mesospheric airglow/aerosol tomography spectroscopy satellite," Appl. Opt. **58**, 1393–1399 (2019).
4. S. Chang and J. A. Prata, "The design of classical offset dragonian reflector antennas with circular apertures," IEEE Trans. Antennas Propag. **52**, 12–19 (2004).
5. S. Chang and J. A. Prata, "Geometrical theory of aberrations near the axis in classical off-axis reflecting telescopes," J. Opt. Soc. Am. A **22**, 2454–2464 (2005).
6. S. Chang, J. H. Lee, S. P. Kim, H. Kim, W. J. Kim, I. Song, and Y. Park, "Linear astigmatism of confocal off-axis reflective imaging systems and its elimination," Appl. Opt. **45**, 484–488 (2006).
7. Q. Wang, L. Tan, J. Ma, S. Yu, and Y. Jiang, "A novel approach for simulating the optical misalignment caused by satellite platform vibration in the ground test of satellite optical communication systems," Opt. Express **20**, 1033–1045 (2012).
8. Y. Cheng, S. J. Mi Wang, L. He, and Y. Tian, "New on-orbit geometric interior parameters self-calibration approach based on three-view stereoscopic images from high-resolution multi-TDI-CCD optical satellites," Opt. Express **26**, 7475–7493 (2018).
9. J. Grodecki and J. Lutes, "IKONOS geometric calibrations," in *Proceedings of the ASPRS 2005 Annual Conference* (2005).
10. M. Wang, Y. Cheng, B. Yang, S. Jin, and H. Su, "On-orbit calibration approach for optical navigation camera in deep space exploration," Opt. Express **24**, 5536–5554 (2016).
11. M. Wang, Y. Cheng, X. Chang, S. Jin, and Y. Zhu, "On-orbit geometric calibration and geometric quality assessment for the high-resolution geostationary optical satellite GaoFen4," ISPRS J. Photogramm. Remote Sens. **125**, 63–77 (2017).
12. N. T. Vo, R. C. Atwood, and M. Drakopoulos, "Preprocessing techniques for removing artifacts in synchrotron-based tomographic images," Proc. SPIE **1113**, 111131I (2019).
13. S. Chang, "Linear astigmatism of confocal off-axis reflective imaging systems with N-conic mirrors and its elimination," J. Opt. Soc. Am. A **32**, 852–859 (2015).
14. S. Kim, S. Pak, S. Chang, G. H. Kim, S. C. Yang, M. S. Kim, S. Lee, and H. Lee, "Proto-model of an infrared wide-field off-axis telescope," J. Korean Astron. Soc. **43**, 169–181 (2010).
15. W. Park, S. Chang, J. H. Lim, S. Lee, H. Ahn, Y. Kim, S. Kim, A. Hammar, B. Jeong, G. H. Kim, H. Lee, D. W. Kim, and S. Pak, "Development of linear astigmatism free—three mirror system (LAF-TMS)," Publ. Astron. Soc. Pac. **132**, 044504 (2020).
16. Q. Wang, D. Cheng, Y. Wang, H. Hua, and G. Jin, "Design, tolerance, and fabrication of an optical see-through head-mounted display with free-form surface elements," Appl. Opt. **52**, C88–C99 (2013).
17. C.-W. Chen and C.-R. Chen, "Optical design and tolerance analysis of a reflecting telescope for CubeSat," Proc. SPIE **9602**, 96020P (2015).
18. B. J. Bauman and M. D. Schneider, "Design of optical systems that maximize as built performance using tolerance/compensator-informed optimization," Opt. Express **26**, 13819–13840 (2018).
19. H. Lee, G. J. Hill, J. L. Marshall, B. L. Vattiat, and D. L. DePoy, "Visible integral-field replicable unit spectrograph (virus) optical tolerance," Proc. SPIE **7735**, 77353X (2010).
20. A. Kuś, "Illumination-related errors in limited-angle optical diffraction tomography," Appl. Opt. **56**, 9247–9256 (2017).

21. J. H. Burge, S. Benjamin, M. Dubin, A. Manuel, M. Novak, C. J. Oh, M. Valente, and C. Zhao, "Development of a wide field spherical aberration corrector for the Hobby Eberly telescope," Proc. SPIE **7733**, 77331J (2010).
22. M. C. Funck and P. Loosen, "The effect of selective assembly on tolerance desensitization," Proc. SPIE **7652**, 76521M (2010).
23. N. Hagen, "Flatfield correction errors due to spectral mismatching," Opt. Eng. **53**, 123107 (2014).
24. D. S. Birney, G. Gonzalez, and D. Oesper, "CCD calibrations," in *Observational Astronomy* (Cambridge University, 2005).
25. G. Giono, G. Olentšenko, N. Ivchenko, O. M. Christensen, J. Gumbel, U. Frisk, A. Hammar, I. Davies, and L. Megner, and the MATS team, "Characterisation of the analogue read-out chain for the CCDs onboard the Mesospheric Airglow/Aerosol Tomography and Spectroscopy (MATS)," Proc. SPIE **10698**, 106984Y (2018).
26. J. E. Harvey, "Parametric analysis of the effect of scattered light upon the modulation transfer function," Opt. Eng. **52**, 073110 (2013).
27. J. Ingers and M. Breidne, "Surface roughness scattering theories—a numerical comparison," Proc. SPIE **1029**, 111–118 (1989).
28. Edmund Optics, "Metallic mirror coatings," https://www.edmundoptics.com.
29. D.-R. Schmitt, "High reflectance low scatter laser mirrors," Proc. SPIE **1125**, 94–106 (1990).
30. W.-K. Park, S. Pak, M. Im, C. Choi, Y. Jeon, S. Chang, H. Jeong, J. Lim, and E. Kim, "Camera for quasars in early universe (CQUEAN)," Publ. Astron. Soc. Pac. **124**, 839–853 (2012).
31. INFRAMET, https://www.inframet.com.
32. H. Fujita, D.-Y. Tsai, T. Itoh, K. Doi, J. Morishita, K. Ueda, and A. Ohtsuka, "A simple method for determining the modulation transfer function in digital radiography," IEEE Trans. Med. Imaging **11**, 34–39 (1992).
33. P. F. Judy, "The line spread function and modulation transfer function of a computed tomographic scanner," Med. Phys. **3**, 233–236 (1976).
34. R. Padgett and C. J. Kotre, "Development and application of programs to measure modulation transfer function, noise power spectrum and detective quantum efficiency," Radiat. Prot. Dosim. **117**, 283–287 (2006).
35. E. Samei, M. J. Flynn, and D. A. Reimann, "A method for measuring the presampled MTF of digital radiographic systems using an edge test device," Med. Phys. **25**, 102–113 (1998).
36. X. Zhang, T. Kashti, D. Kella, T. Frank, D. Shaked, R. Ulichney, M. Fischer, and J. P. Allebach, "Measuring the modulation transfer function of image capture devices: what do the numbers really mean?" Proc. SPIE **8293**, 829307 (2012).
37. S. Chang, "Elimination of linear astigmatism in off-axis three-mirror telescope and its applications," Proc. SPIE **8860**, 88600U (2013).